Chemical Science

ROYAL SOCIETY OF CHEMISTRY

EDGE ARTICLE

View Article Online
View Journal | View Issue



Cite this: *Chem. Sci.*, 2025, **16**, 22732

All publication charges for this article have been paid for by the Royal Society of Chemistry



# A cation gating–breathing synergetic mechanism in K-MER-2.0 zeolite enables unprecedented selective $CO_2$ separation from hydrocarbon gas streams

Renhao Li,†[a] Chenxu Liu,†[a] Wenli Bao,[b] Lin Li,[c] Jingfeng Han,[d] Xiaoxin Zou,[a] Xiaowei Song,*[a] Donghai Mei*[b] and Zhiqiang Liang*[a]

Received 6th May 2025
Accepted 12th October 2025

DOI: 10.1039/d5sc03281d

rsc.li/chemical-science

The ubiquitous presence of $CO_2$ impurities in industrial hydrocarbon streams underscores the critical need for developing efficient $CO_2$-selective adsorbents. Herein, we synthesized a flexible K-MER-2.0 (a silica–alumina ratio of 2.0) zeolite without using an organic template, which demonstrates exceptional selective adsorption performance in $CO_2$/hydrocarbon systems, and in particular achieves the unprecedented reverse separation of $CO_2/C_2H_2$. K-MER exhibits a $CO_2$ adsorption capacity of 70.9 $cm^3$ $g^{-1}$ under ambient conditions, accompanied by a remarkable $CO_2/C_2H_2$ uptake ratio (13.4). Breakthrough experiments conducted with a $CO_2/C_2H_2$ (50/50, v/v) mixture reveal that K-MER-2.0 delivers a high dynamic $CO_2$ adsorption capacity (65.1 $cm^3$ $g^{-1}$) and separation factor (12.1), and in particular a high $C_2H_2$ yield of 1872 mmol $kg^{-1}$, establishing a benchmark for $CO_2/C_2H_2$ reverse separation. The rapid adsorption kinetics, excellent regeneration and robust moisture resistance of K-MER-2.0 further confirmed its application potential under harsh practical conditions. Mechanistic analyses, including $CO_2/C_2H_2$ adsorption isotherms, *in situ* $CO_2$ powder X-ray diffraction (PXRD) patterns and periodic density functional theory (DFT) calculations, reveal a unique $CO_2$-triggered cation gating–breathing synergetic mechanism in K-MER-2.0 zeolite. This stimulus-responsive mechanism facilitates selective framework expansion during $CO_2$ adsorption while preserving a constricted pore geometry that excludes $C_2H_2$. Such discriminative structural adaptability drives the record-breaking separation performance of the material. Additionally, the unique recognition ability for $CO_2$ endows K-MER-2.0 with good dynamic separation ability for binary mixtures of $CO_2$/hydrocarbons.

## Introduction

The strategic significance of developing advanced $CO_2$/hydrocarbon separation technologies arises from two fundamental industrial considerations: (1) hydrocarbon gases (including $C_2H_2$, $C_2H_4$, $C_2H_6$, $C_3H_6$, $C_3H_8$, and $CH_4$) serve as critical feedstocks and energy vectors, and (2) $CO_2$ invariably coexists in hydrocarbon product streams as a ubiquitous impurity.[1] $C_2H_2/CO_2$ separation represents one of the most challenging gas purification processes in petrochemical systems, primarily due to their nearly identical molecular properties, including comparable polarities (33.3 $\times 10^{-25}$ $cm^3$ for $C_2H_2$ *vs.* 29.1 $\times 10^{-25}$ $cm^3$ for $CO_2$), similar kinetic diameters (3.3 Å for both), and overlapping adsorption affinities.[2–4] Conventional industrial methods predominantly employ organic-solvent-based absorption systems and cryogenic distillation operations, which suffer from significant energy consumption.[4] This has driven the increasing adoption of physisorption-based separation platforms that offer distinct advantages in energy efficiency (>30% reduction in energy consumption), rapid adsorption–desorption kinetics, and exceptional cycling stability.[5–7] Notably, the energy efficiency of $CO_2$-selective adsorbents ($CO_2/C_2H_2$ reverse separation) increases by 40% compared to that of $C_2H_2$-selective alternatives ($C_2H_2/CO_2$ positive separation) in separation processes, highlighting the potential for sustainable hydrocarbon purification.[1] This advantage arises primarily from $CO_2/C_2H_2$ reverse separation, which facilitates the direct acquisition of pure $C_2H_2$ product while obviating the need for energy-intensive multistep desorption processes.

The key to achieving efficient $CO_2/C_2H_2$ reverse separation is the design and synthesis of advanced porous adsorbents. In the

[a]*State Key Lab of Inorganic Synthesis and Preparative Chemistry, College of Chemistry, Jilin University, Changchun, 130012, P. R. China. E-mail: xiaoweisong@jlu.edu.cn; liangzq@jlu.edu.cn*

[b]*School of Materials Science and Engineering, Tiangong University, Tianjin, 300387, P. R. China. E-mail: dhmei@tiangong.edu.cn*

[c]*Electron Microscopy Centre, Jilin University, Changchun 130012, P. R. China*

[d]*National Engineering Research Center of Lower-Carbon Catalysis Technology, Dalian Institute of Chemical Physics, Chinese Academy of Sciences, Dalian 116023, P. R. China*

† R. Li and C. Liu contributed equally to this work.

past decade, metal–organic frameworks (MOFs) have attracted considerable research interest for $CO_2/C_2H_2$ reverse separation, with notable examples including Zn-ox-mtz,[8] MUF-16,[9] PCP-$NH_2$-bdc,[10] and PMOF-1.[11] However, their practical implementation in gas separation technologies has been constrained by persistently high synthesis costs and relatively poor stability.[12] This economic limitation has driven the increasing attention paid to zeolite-based materials, which offer distinct advantages in terms of cost-effectiveness, industrial scalability, structural stability, and high thermal/hydrothermal stability.[4] Recent studies have demonstrated the potential of zeolites in this domain, exemplified by Sr/K-HEU achieving a dynamic $CO_2/C_2H_2$ separation factor of 48.0 and $CO_2$ dynamic uptake of 21.5 $cm^3\ g^{-1}$.[13] Furthermore, Na-GIS(3.1) has shown selective $CO_2$ adsorption in $CO_2/C_2H_2$ mixtures, accompanied by a pure $C_2H_2$ yield of 100 mmol $kg^{-1}$.[14] In addition, $NaAlO_2$@MOR(0.5) also exhibited a remarkable kinetic separation selectivity of 534.3.[15] Among zeolitic materials, K-MER has emerged as particularly promising due to its flexible framework and unique adsorption mechanisms, particularly for $CO_2/N_2$ and $CO_2/CH_4$ mixed systems. *In situ* $CO_2$ variable-pressure synchrotron powder X-ray diffraction coupled with Rietveld refinement have revealed that K-MER exhibited a unique cation gating–breathing synergistic mechanism during $CO_2$ adsorption.[16–19] This dual-action mechanism differs from the "trapdoor" effect observed in Sr/K-HEU,[13] the monofunctional breathing behaviour of Na-GIS(3.1),[14] and the kinetic separation of $NaAlO_2$@-MOR(0.5).[15] However, it has rarely been reported that the pore architecture of K-MER retains closure not only towards low-polar gases ($N_2$, $CH_4$) but also extends to high-polar hydrocarbons (*e.g.*, $C_2H_2$, $C_2H_4$, $C_2H_6$, $C_3H_6$, and $C_3H_8$). Despite this critical property, systematic investigation of the potential of K-MER for $CO_2$/hydrocarbon separation applications remains notably underexplored, creating a substantial gap in the understanding of its gas separation applications.

Herein, we report an organic-template-free synthesized K-MER-2.0 zeolite (a silica–alumina ratio of 2.0) that exhibits a remarkable $CO_2$ static adsorption capacity of 70.9 $cm^3\ g^{-1}$ at 298 K and 101 kPa, significantly outperforming its hydrocarbon adsorption capacities, and thereby demonstrating exceptional $CO_2$/hydrocarbon separation performance. This material achieves an ideal adsorbed solution theory (IAST) selectivity of 3056 for $CO_2/C_2H_2$ (50/50, v/v) mixtures. Notably, K-MER-2.0 enables the single-step purification of acetylene with a remarkably high $C_2H_2$ productivity of 1872 mmol $kg^{-1}$ in breakthrough experiments, eliminating the need for multi-stage desorption processes and serving as a benchmark for a zeolite-based adsorbent. Meanwhile, the dynamic adsorption capacity of $CO_2$ reached 65.1 $cm^3\ g^{-1}$, accompanied by a separation factor of 12.1. The material demonstrates rapid adsorption kinetics (1.7 min to reach $CO_2$ uptake of 43.7 mg $g^{-1}$), exceptional moisture tolerance (73.9% $C_2H_2$ production under 50% relative humidity), and a low regeneration temperature (353 K). Comparative analyses of $CO_2/C_2H_2$ adsorption isotherms, *in situ* $CO_2$ powder X-ray diffraction (PXRD) patterns, and periodic density functional theory (DFT) calculations reveal a unique $CO_2$-triggered cation gating–breathing synergetic mechanism. This stimuli-responsive framework maintains a rigid structure for hydrocarbons while exhibiting $CO_2$-induced framework flexibility, enabling molecular discrimination through dynamic pore modulation. This work advances a fundamental understanding of cation-mediated framework flexibility and establishes a novel strategy for developing smart zeolite materials with selective framework-breathing and gate-opening functionalities for challenging gas separations.

## Results and discussion

### Characterizations of K-MER-2.0 zeolites

Utilizing KOH as the exclusive alkaline medium, K-MER-2.0 zeolite was successfully synthesized in an organic-template-free system. The powder X-ray diffraction (PXRD) pattern of as-synthesized K-MER-2.0 zeolite was almost consistent with a simulated one of MER-type zeolite, except for the distinctive diffraction peaks at 26.0° and 29.7° (Fig. 1a), which were induced by symmetry reduction from the *Immm* space group (no. 71) of a typical MER framework to a lower-symmetry *Pnnm* space group (no. 58), rather than arising from phase impurities.[20,21] Scanning/transmission electron microscopy (SEM/TEM) images showed the as-synthesized K-MER-2.0 zeolite existed in the form of micron-sized rod-like aggregations (Fig. S1, S2 and Table S1). The coordination environment of framework elements was elucidated through $^{29}Si/^{27}Al$ solid-state magic angle spinning nuclear magnetic resonance (MAS NMR) analysis (Fig. 1b and S3). Four distinct strong signals at −91, −96, −101, and −107 ppm in the $^{29}Si$ MAS NMR spectrum were attributed to $Si(OSi)_4$ ($Q_4$), $Si(OSi)_3(OAl)$ ($Q_4$), $Si(OSi)_2(OAl)_2$ ($Q_4$), and $Si(OSi)(OAl)_3$ ($Q_4$), respectively, indicating the good crystallization of K-MER-2.0. The $^{27}Al$ solid-state MAS NMR spectrum demonstrated that the aluminum species in the as-synthesized K-MER-2.0 existed exclusively in a tetrahedral coordination state (60.5 ppm) without the presence of extra-framework aluminum species (0 ppm). Complementary $^{13}C$ solid-state CP/MAS NMR spectrum (Fig. 1c) and thermogravimetric analysis (Fig. S4) confirmed no residual oxalic acid in the as-synthesized K-MER-2.0 zeolite. These findings suggest that oxalic acid functions primarily as a pH modulator and mineralizer complexing agent (with $K^+$), rather than acting as a structure-directing template.[22] Elemental mapping *via* TEM-EDS (Fig. 1d–h) further verified the homogeneous distribution of $K^+$ within the pore channels. To investigate cation effects on structural stability and gas adsorption properties, ion-exchanged derivatives (Li-MER-2.0, Na-MER-2.0, and Cs-MER-2.0) were prepared from K-MER-2.0 through cation exchange followed by calcination (Fig. 1a and Table S1). Na-MER-2.0 maintained both MER topology and crystallinity comparable to the parent K-MER-2.0, while Cs-MER-2.0 exhibited minor framework degradation during the ion exchange process. In contrast, Li-MER-2.0 showed significant attenuation in PXRD peak intensity, attributed to the insufficient framework stabilization by smaller $Li^+$ ions in the flexible MER architecture.[17,18] Consequently, subsequent analyses focused on the more stable Na-MER-2.0, K-MER-2.0, and Cs-MER-2.0 variants. Meanwhile, for Na-MER-2.0 and Cs-MER-2.0, SEM images confirmed the

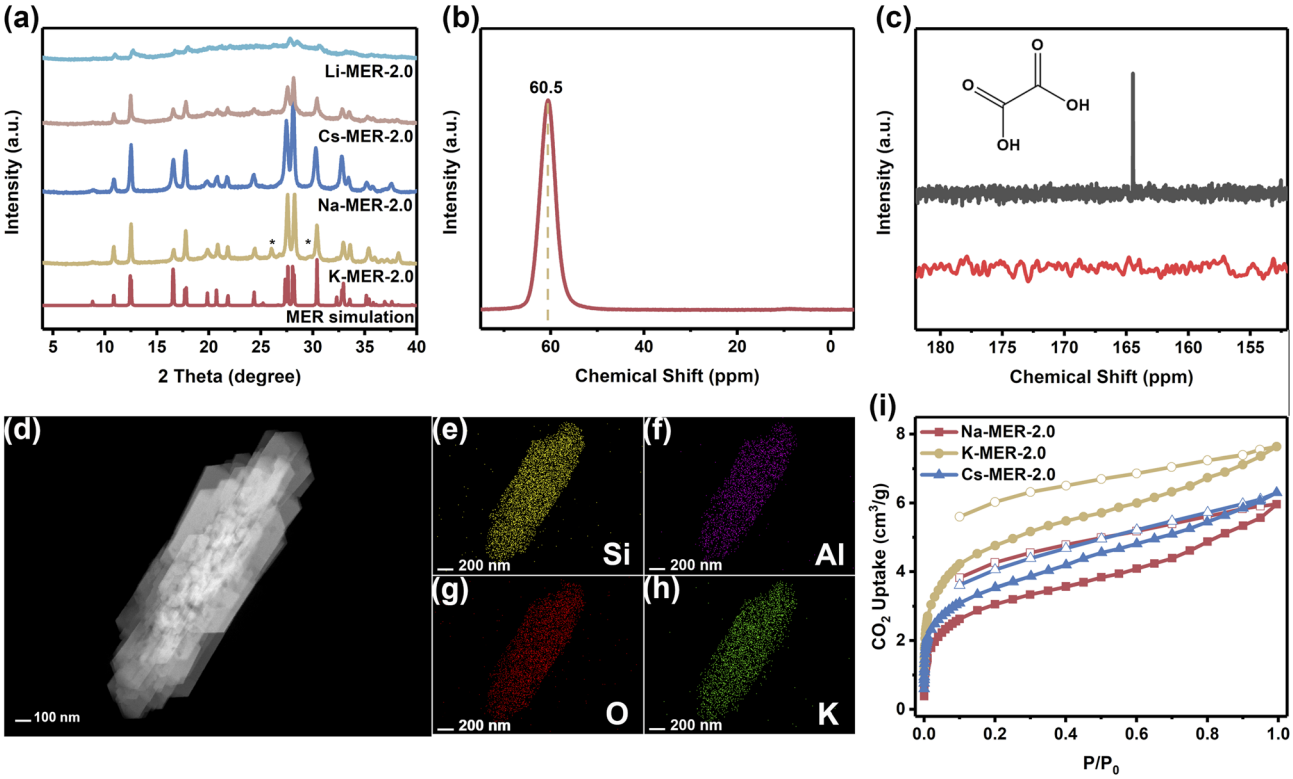


Fig. 1 (a) The simulated PXRD pattern of MER zeolite and experimental patterns of K-MER-2.0, Na-MER-2.0, Cs-MER-2.0, and Li-MER-2.0. (b) The solid-state $^{27}$Al MAS NMR spectrum of K-MER-2.0. (c) The liquid-state $^{13}$C NMR spectrum of oxalic acid dissolved in $D_2O$ (top curve, black) and the solid-state $^{13}$C MAS NMR spectrum of the as-synthesized K-MER-2.0 after washing with deionized water (bottom curve, red). (d) An TEM image of K-MER-2.0. (e–h) Elemental mapping *via* TEM-EDS of K-MER-2.0 for Si (e), Al (f), O (g), and K (h). (i) The $CO_2$ adsorption isotherms of Na-MER-2.0, K-MER-2.0, and Cs-MER-2.0 at 195 K.

preservation of morphological features during ion exchange (Fig. S5), and $^{27}$Al solid-state MAS NMR spectra confirmed the absence of extra-framework Al species (Fig. S6 and S7).

It is well known that the adsorption capacity of porous materials is critically influenced by their specific surface area and pore volume.[23] However, the adsorption isotherms of $N_2$ ($d$ = 0.36 nm) at 77 K and Ar ($d$ = 0.34 nm) at 87 K revealed that only a few $N_2$ and Ar molecules could be adsorbed into the micropores of K-MER-2.0, Na-MER-2.0, and Cs-MER-2.0 (Fig. S8 and S9). This observation suggests that the flexible framework of K-MER-2.0 maintains a contracted configuration under nitrogen or argon atmospheres.[16] To further investigate this size exclusion effect, we conducted $CO_2$ ($d$ = 0.33 nm) adsorption measurements at 195 K. Surprisingly, despite its smaller kinetic diameter, the $CO_2$ adsorption amounts of all three MER-type zeolites were still less than 8 cm$^3$ g$^{-1}$ (Fig. 1i). We propose that this anomalous exclusion behavior stems primarily from the suppressed thermal motion of charge-balancing cations within the zeolite pores at cryogenic temperatures. The reduced cation vibration elevates the energy barrier for cation migration, effectively maintaining a rigid pore structure that prevents gas molecule penetration. This phenomenon aligns with the temperature-dependent adsorption behavior observed in LTA-type zeolites, which adsorb $N_2$ at room temperature but exhibit non-adsorbent characteristics at 77 K.[24]

Compared to the $CO_2$ adsorption isotherm observed at 195 K, the K-MER-2.0 zeolite demonstrated significantly enhanced $CO_2$ adsorption performance at 298 K with a remarkable adsorption capacity of 70.9 cm$^3$ g$^{-1}$ at 101 kPa and a steep adsorption curve within the low-pressure region (1 kPa: 37.8 cm$^3$ g$^{-1}$, 10 kPa: 52.6 cm$^3$ g$^{-1}$) (Fig. 2a and Table S2). The quasi-reversible nature of $CO_2$ adsorption was confirmed by the nearly overlapping adsorption–desorption isotherms. Simultaneously, a critical structural transition was identified at 0.4 kPa (298 K), marked by an inflection point in the $CO_2$ adsorption curve and a subsequent sharp increase in adsorption capacity (Fig. S10). This phenomenon indicates a pressure-induced framework transformation from a contracted to an expanded state in the K-MER-2.0 structure, which has been observed in PHI topology molecular sieves.[25] In stark contrast, K-MER-2.0 displayed ultra-low adsorption capacities for various hydrocarbon gases at 298 K and 101 kPa, with uptakes of 5.3 cm$^3$ g$^{-1}$ for $C_2H_2$, 1.3 cm$^3$ g$^{-1}$ for $C_2H_4$, 0.6 cm$^3$ g$^{-1}$ for $C_2H_6$, 2.7 cm$^3$ g$^{-1}$ for $C_3H_6$, 3.3 cm$^3$ g$^{-1}$ for $C_3H_8$, and 0.04 cm$^3$ g$^{-1}$ for $CH_4$ (Fig. 2a and Table S2). The ultra-low adsorption capacities and the absence of inflection points in these hydrocarbon isotherms suggest that the framework maintains its contracted conformation during hydrocarbon gas adsorption. This salient adsorption selectivity establishes K-MER-2.0 as an exceptional molecular sieve material for $CO_2$/hydrocarbon separation, with impressive adsorption capacity ratios at 298 K and 101 kPa: 13.4 ($CO_2/C_2H_2$), 54.5

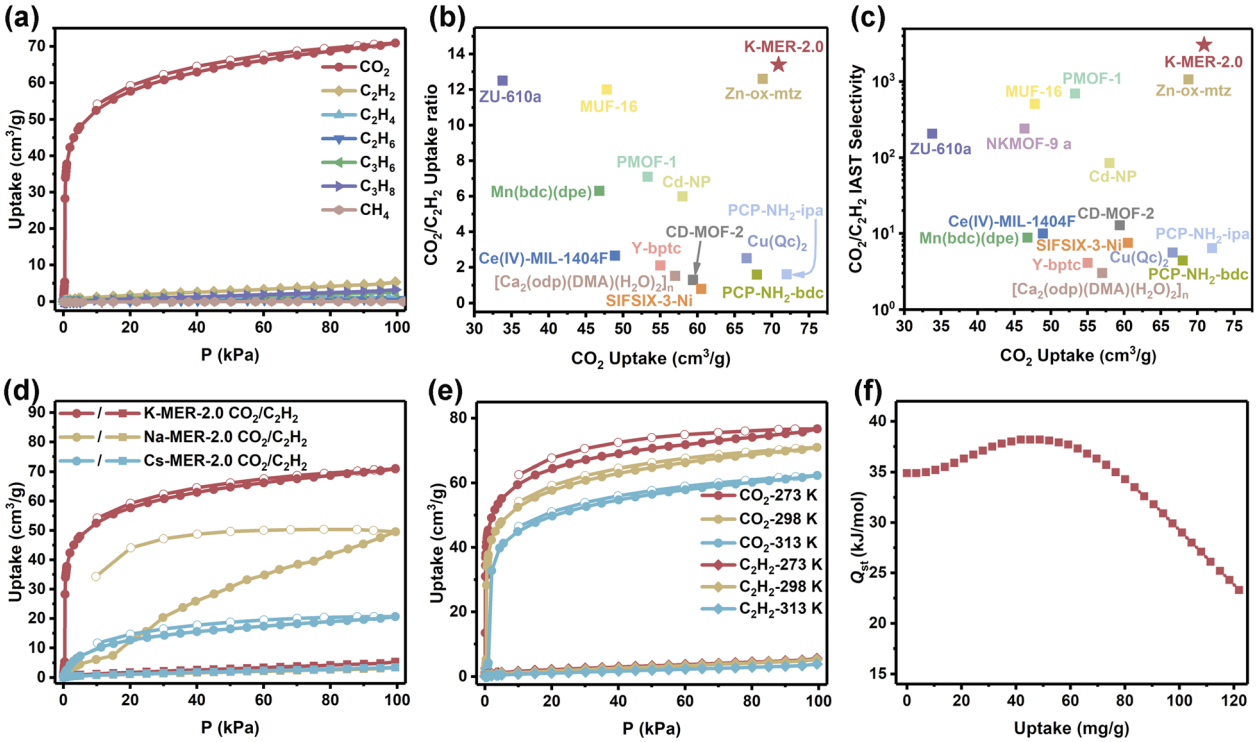


Fig. 2 A comparison of static adsorption performance. (a) Static sorption curves of $CO_2$, $C_2H_2$, $C_2H_4$, $C_2H_6$, $C_3H_6$, $C_3H_8$, and $CH_4$ for K-MER-2.0 at 298 K. (b) A comparison of the $CO_2/C_2H_2$ uptake ratio and $CO_2$ uptake of state-of-the-art materials (101 kPa, 298 K). (c) A comparison of $CO_2/C_2H_2$ (50/50, v/v) IAST selectivity and $CO_2$ uptake (101 kPa, 298 K) of state-of-the-art materials. (d) Static sorption curves of $CO_2$ and $C_2H_2$ for Na-MER-2.0, K-MER-2.0, and Cs-MER-2.0 at 298 K. (e) Static sorption curves of $CO_2$ and $C_2H_2$ for K-MER-2.0 at 273, 298 and 313 K. (f) $CO_2$ adsorption enthalpies ($Q_{st}$) of K-MER-2.0.

($CO_2/C_2H_4$), 118.2 ($CO_2/C_2H_6$), 26.3 ($CO_2/C_3H_6$), 21.3 ($CO_2/C_3H_8$), and 1772.5 ($CO_2/CH_4$) (Table S2).

It is well established that among various hydrocarbons, $C_2H_2$ exhibits physicochemical properties and a kinetic diameter most closely resembling those of $CO_2$.[4,12] The high adsorption capacity ratio of $CO_2/C_2H_2$ indicates that the K-MER-2.0 zeolite is particularly suitable for selective $CO_2$ capture from the $CO_2/C_2H_2$ separation system to produce pure $C_2H_2$. Remarkably, K-MER-2.0 demonstrated exceptional separation efficiency with an IAST selectivity of 3056 for the $CO_2/C_2H_2$ (50/50, v/v) system (Fig. S11). As shown in Fig. 2b, c and Table S4, K-MER-2.0 exhibited superior performance metrics in reverse $CO_2/C_2H_2$ separation: $CO_2$ uptake (70.9 $cm^3\ g^{-1}$), uptake ratio (13.4), and IAST selectivity (3056), significantly surpassing current benchmark materials. These values notably exceed those of state-of-the-art materials, including Zn-ox-mtz (68.78 $cm^3\ g^{-1}$; 12.6; 1064.9),[8] MUF-16 (48 $cm^3\ g^{-1}$; 12.0; 510),[8] and PMOF-1 (53.3 $cm^3\ g^{-1}$; 7.1; 694).[11] Comparative analysis with other cation-exchanged MER frameworks revealed distinct differences in performance (Fig. 2d). K-MER-2.0 demonstrated a $CO_2$ adsorption capacity of 70.9 $cm^3\ g^{-1}$ with reversible adsorption and favorable low-pressure adsorption characteristics, while Na-MER-2.0 showed reduced capacity (49.6 $cm^3\ g^{-1}$) accompanied by an adsorption isotherm inflection point shift to 7.5 kPa and significant adsorption–desorption hysteresis. These characteristics substantially compromised the separation performance of Na-MER-2.0, despite its comparable uptake ratio (14.6) to K-MER-2.0. Cs-MER-2.0 exhibited even poorer performance with $CO_2$ uptake of 20.6 $cm^3\ g^{-1}$ and a low uptake ratio of 5.9 (Table S3).

Thermodynamic analysis through variable-temperature adsorption isotherms revealed a zero-coverage $CO_2$ adsorption enthalpy ($Q_{st}$) of 34.9 kJ $mol^{-1}$ for K-MER-2.0 (Fig. 2e and f). This physisorption-dominated mechanism, evidenced by the moderate $Q_{st}$ value, facilitates material regeneration compared to frameworks with higher enthalpies, such as NKMOF-9a (69.5 kJ $mol^{-1}$)[26] and CD-MOF-2 (67.2 kJ $mol^{-1}$)[27] (Table S4). Notably, the $CO_2$ adsorption enthalpy profile of K-MER-2.0 exhibited an atypical trend of an initial increase followed by a gradual decline (Fig. 2f), which we attribute to the limited pore accessibility and shielding effects on high-energy adsorption sites at low $CO_2$ loadings. The temperature-dependent adsorption behavior showed systematic shifts in isotherm inflection points from 0.04 kPa (273 K) to 1.0 kPa (313 K) (Fig. S12), consistent with established gas adsorption thermodynamics.[28] This predictable temperature response further supports the potential of K-MER-2.0 for practical separation applications under varying operational conditions.

The $CO_2$ adsorption kinetics of K-MER-2.0 were systematically investigated under varying pressure conditions (15, 50 and 96 kPa), as shown in Fig. S13. Under low-pressure conditions (15 kPa), the adsorption capacity demonstrated rapid initial uptake, reaching 43.7 mg $g^{-1}$ (22.2 $cm^3\ g^{-1}$) within 1.7 minutes, followed by gradual equilibration to a maximum capacity of

102.2 mg $g^{-1}$ (52.0 $cm^3$ $g^{-1}$) over 15 minutes. In contrast, when subjected to elevated pressures (50 and 96 kPa), the system exhibited instantaneous equilibrium characteristics upon pressure stabilization, achieving $CO_2$ adsorption capacities of 119.6 mg $g^{-1}$ (60.9 $cm^3$ $g^{-1}$) and 128.7 mg $g^{-1}$ (65.5 $cm^3$ $g^{-1}$), respectively. This pressure-dependent kinetic behavior highlights the rapid adsorption response of the material at higher pressures, which significantly enhances separation efficiency by minimizing the unnecessary consumption of selective adsorption capacity during non-productive stages involving simultaneous gas permeation.[23] The distinct kinetic profiles observed under different pressure conditions provide critical insights for optimizing operational parameters in gas separation applications.

To investigate the impact of the Si/Al ratio on $CO_2/C_2H_2$ separation performance in K-MER, we synthesized K-MER samples with other Si/Al ratios of 2.7 and 3.8, denoted K-MER-2.7 and K-MER-3.8 (Fig. S14 and Table S1). The decreased $K^+$ content resulting from higher Si/Al ratios increases the void volume of MER zeolites, boosting the static $CO_2$ adsorption capacity from 70.9 $cm^3$ $g^{-1}$ (K-MER-2.0) to 75.9 $cm^3$ $g^{-1}$ (K-MER-2.7) and 85.2 $cm^3$ $g^{-1}$ (K-MER-3.8) (Fig. S15). Meanwhile, the reduction of $K^+$ content in the pore of the MER zeolite weakens the interactions between $K^+$ and the zeolite framework, causing the $CO_2$ adsorption inflection point to shift from 0.4 kPa (K-MER-2.0) to 0.1 kPa (K-MER-2.7), with a further decline to below 0.02 kPa for K-MER-3.8 (Fig. S16). However, the $C_2H_2$ adsorption capacity significantly increases from 5.3 $cm^3$ $g^{-1}$ (K-MER-2.0) to 11.3 $cm^3$ $g^{-1}$ (K-MER-2.7) and 52.3 $cm^3$ $g^{-1}$ (K-MER-

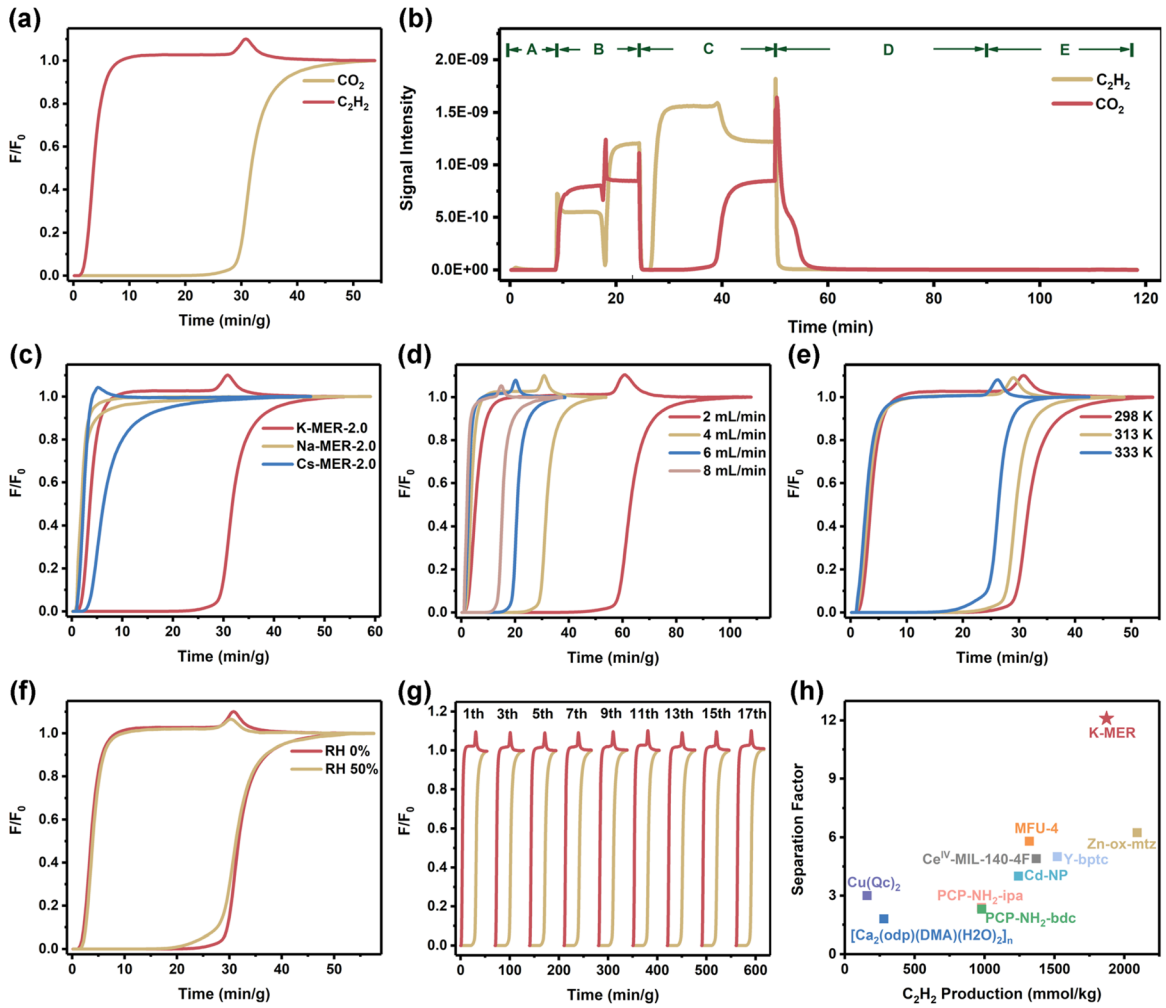


Fig. 3 Column breakthrough studies of a $CO_2/C_2H_2$ separation system using K-MER-2.0. (a) Experimental breakthrough curves of K-MER-2.0 for $CO_2/C_2H_2$ (50/50, v/v) mixtures at 298 K with a flow rate of 4 mL $min^{-1}$. (b) Mass spectrum signal curves of $CO_2/C_2H_2$ over the whole K-MER-2.0 measurement process. A: sample activation process; B: signal stabilization process of $CO_2/C_2H_2$ before breakthrough measurement; C: breakthrough measurement process (298 K); D: desorption process of the sample accompanied by 25 mL per min helium at 353 K; E: desorption process when the temperature started to rise to 473 K and remained there for 20 min. (c) A comparison of breakthrough curves of K-MER-2.0, Na-MER-2.0, and Cs-MER-2.0 for $CO_2/C_2H_2$ (50/50, v/v) mixtures at 298 K with a flow rate of 4 mL $min^{-1}$. (d) Breakthrough curves for $CO_2/C_2H_2$ (50/50, v/v) mixtures at 298 K with flow rates of 2, 4, 6, and 8 mL $min^{-1}$. (e) Breakthrough curves for $CO_2/C_2H_2$ (50/50, v/v) mixtures at 298 K, 313 K, and 333 K with a flow rate of 4 mL $min^{-1}$. (f) Effects of $H_2O$ (RH = 50%) on $CO_2/C_2H_2$ (50/50, v/v) separation at 298 K with a flow rate of 4 mL $min^{-1}$ (g) A study of recyclability for the separation of $CO_2/C_2H_2$ (50/50, v/v) at 298 K with a flow rate of 4 mL $min^{-1}$. Sample regeneration was achieved by treatment in helium at 353 K. (h) A comparison of separation factor and pure $C_2H_2$ production of state-of-the-art materials.

3.8) (Fig. S15). Consequently, the $CO_2/C_2H_2$ adsorption ratio decreases from 13.4 (K-MER-2.0) to 6.7 (K-MER-2.7) and 1.6 (K-MER-3.8) (Table S5). The increase in Si/Al ratios reduces pore blockage in K-MER zeolites, allowing $C_2H_2$ adsorption to occur—a phenomenon consistent with previous literature.[22] Overall, K-MER-2.0 exhibited significantly superior separation performance compared to K-MER-2.7 and K-MER-3.8.

To evaluate the practical separation performance of K-MER-2.0 under realistic flow conditions, dynamic breakthrough experiments were conducted using a $CO_2/C_2H_2$ (50/50, v/v) gas mixture at a total flow rate of 4 mL $min^{-1}$, following established protocols in gas separation studies (Fig. 3a).[29] The breakthrough curves revealed distinct adsorption behaviors: $C_2H_2$ exhibited rapid breakthrough at 1.0 min $g^{-1}$ with subsequent saturation, while $CO_2$ demonstrated prolonged retention with a breakthrough time of 24.4 min $g^{-1}$. Quantitative analysis yielded dynamic adsorption capacities of 65.1 $cm^3$ $g^{-1}$ for $CO_2$ and 5.4 $cm^3$ $g^{-1}$ for $C_2H_2$, corresponding to an impressive separation factor ($\alpha$) of 12.1 (Table S6). Notably, K-MER-2.0 achieved the direct production of high-purity $C_2H_2$ (99.6%) with a yield of 1872 mmol $kg^{-1}$ through single-step adsorption, eliminating the requirement for energy-intensive thermal desorption processes. Comparative performance analysis with state-of-the-art adsorbents highlights the superior separation characteristics of K-MER-2.0. Although Zn-ox-mtz (a leading MOF material) shows marginally higher $C_2H_2$ productivity (2091 mmol $kg^{-1}$),[18] K-MER-2.0 demonstrates a two-fold enhancement in separation factor (12.1 *vs.* 6.24), significantly reducing acetylene loss during separation cycles (Fig. 3h and Table S7). Furthermore, K-MER-2.0 outperforms other benchmark materials, including Ce(IV)-MIL-140-4F (1370 mmol $kg^{-1}$, $\alpha$ = 4.9),[30] Y-bptc (1520 mmol $kg^{-1}$, $\alpha$ = 5),[31] MFU-4 (1320 mmol $kg^{-1}$, $\alpha$ = 5.8),[32] and Cd-NP (1242 mmol $kg^{-1}$, $\alpha$ = 4),[33] establishing it as the current performance leader among previously reported porous adsorbents, including MOFs and zeolites. (Table S7). Regeneration studies demonstrated exceptional desorption properties: complete $CO_2$ release occurred within 10 min under He purging at 353 K, with $C_2H_2$ signals dissipating immediately upon initiation of desorption (Fig. 3b). Subsequent temperature-programmed desorption to 473 K confirmed the absence of residual adsorbates *via* mass spectrometry, demonstrating full regenerability. This facile regeneration behavior aligns with the low $CO_2$ adsorption enthalpy of the material and reversible adsorption isotherms, suggesting minimal energy requirements for cyclic operation, which is a critical advantage for industrial implementation.

Compared to K-MER-2.0 (23.4 min $g^{-1}$), the $CO_2/C_2H_2$ breakthrough time differentials for Na-MER-2.0 and Cs-MER-2.0 significantly decreased to 0.35 and 1.79 min $g^{-1}$, respectively (Fig. 3c). Notably, K-MER-2.0 demonstrated superior separation performance with a pure $C_2H_2$ yield of 1872 mmol $kg^{-1}$ and separation factor of 12.1, substantially exceeding those of Na-MER-2.0 (0.015 mmol $kg^{-1}$, 1.4) and Cs-MER-2.0 (47 mmol $kg^{-1}$, 3.6). These remarkable disparities established K-MER-2.0 as the optimal candidate for subsequent investigations. Systematic evaluation revealed that K-MER-2.0 maintained consistent $CO_2$ dynamic adsorption capacities between 63.8 and 65.1 $cm^3$ $g^{-1}$ across flow rates spanning 2–8 mL $min^{-1}$ (Fig. 3d). Thermal stability tests showed that the $C_2H_2$ productivity remained 1291 mmol $kg^{-1}$ (69.0% retention) even at 333 K (Fig. 3e). Addressing the well-documented moisture sensitivity of zeolites,[23] K-MER-2.0 exhibited exceptional humidity tolerance, retaining 80.0% of its $CO_2$ breakthrough time and 73.9% $C_2H_2$ production capacity under 50% relative humidity (Fig. 3f). Furthermore, the material demonstrated excellent regeneration stability through seventeen consecutive adsorption–desorption cycles (desorption at 353 K), with negligible variation in $CO_2/C_2H_2$ breakthrough profiles (Fig. 3g). The excellent cycling stability of K-MER-2.0 was also preserved under humid conditions (Fig. S17).

To systematically validate the universality of K-MER-2.0 in $CO_2$/hydrocarbon separation, we performed dynamic breakthrough experiments using isovolumetric binary mixtures of $CO_2/C_2H_4$, $CO_2/C_2H_6$, and $CO_2/CH_4$ under a constant total flow rate of 4 mL $min^{-1}$ (Fig. 4a–c and Table S8). The separation performance exhibited remarkable consistency across different hydrocarbon systems. For the $CO_2/C_2H_4$ separation system, K-MER-2.0 demonstrated a $CO_2$ dynamic adsorption capacity of 64.8 $cm^3$ $g^{-1}$, achieving ethylene purification with 99.6% purity (1663 mmol $kg^{-1}$ yield) and a separation factor of 27.3. In the $CO_2/C_2H_6$ system, comparable $CO_2$ uptake capacity (65.1 $cm^3$ $g^{-1}$) was observed while maintaining an ethane purity of 99.6% (1789 mmol $kg^{-1}$ yield), with a separation factor of 19.3. Similarly, in the $CO_2/CH_4$ separation experiments, the material

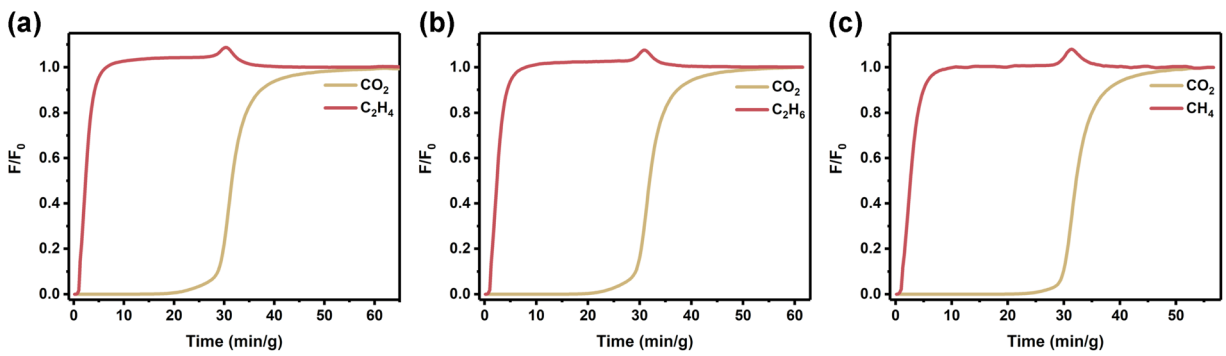


Fig. 4 Studies on the universality of K-MER-2.0 for separating $CO_2$ from other hydrocarbon mixtures. (a–c) Experimental breakthrough curves for isovolumetric $CO_2/C_2H_4$ (a), $CO_2/C_2H_6$ (b), and $CO_2/CH_4$ (c) mixtures at 298 K with a flow rate of 4 mL $min^{-1}$.

showed enhanced $CO_2$ capture capacity (66.1 $cm^3$ $g^{-1}$) accompanied by methane purification to 99.6% purity (1992 mmol $kg^{-1}$ yield) and a separation factor of 13.9. These comprehensive results, supported by both static adsorption isotherms and dynamic breakthrough analyses, establish that K-MER-2.0 possesses exceptional versatility in gas separation applications. The material not only enables the reverse separation of $CO_2/C_2H_2$, but it also demonstrates superior separation performance for $CO_2$ removal from various hydrocarbon systems, including light alkenes ($C_2H_4$), alkanes ($C_2H_6$), and methane ($CH_4$).

The adsorption mechanisms of $CO_2$ in K-MER-2.0 have been systematically investigated through *in situ* $CO_2$ powder X-ray diffraction coupled with the static $CO_2$ adsorption isotherms. Notably, the flexible framework of K-MER-2.0 demonstrates a distinct structural transition from a contracted to an expanded state during $CO_2$ adsorption, as evidenced by characteristic inflection points in both static adsorption isotherms and *in situ* $CO_2$ PXRD patterns (Fig. S10 and S18). Meanwhile, it has been covered extensively in previous reports that this structural transformation is accompanied by specific cation migration events: $K^+$ ions relocate from initial positions at sites Ia (within the *d8r* cage) and sites II (in the *s8r*s between *pau* and *ste* cages) to energetically favorable positions at sites I (in the *s8r*s between *d8r* and *pau* cages) and sites III (in the *s8r*s between two adjacent *ste* cages) (Fig. S19).[17,18,34–36] This concerted framework-cation interaction has been formally described as a cooperative cation-gated breathing mechanism.[17] In striking contrast, $C_2H_2$ adsorption studies reveal fundamentally different behavior. The K-MER-2.0 framework maintains its contracted configuration throughout $C_2H_2$ exposure, as demonstrated by both the absence of inflection points in static adsorption isotherms and the negligible $C_2H_2$ uptake capacity of the material (5.3 $cm^3$ $g^{-1}$) (Fig. 2a and Table S2). Periodic density functional theory (DFT) calculations were used to further explain the unique recognition ability of K-MER-2.0 towards $CO_2$. As shown in Fig. S20, the energy barrier for the transition from $C_2H_2$ adsorption on the contracted K-MER-2.0 framework to the expanded framework was 191.0 kJ $mol^{-1}$. In contrast, the energy barrier associated with the transition from

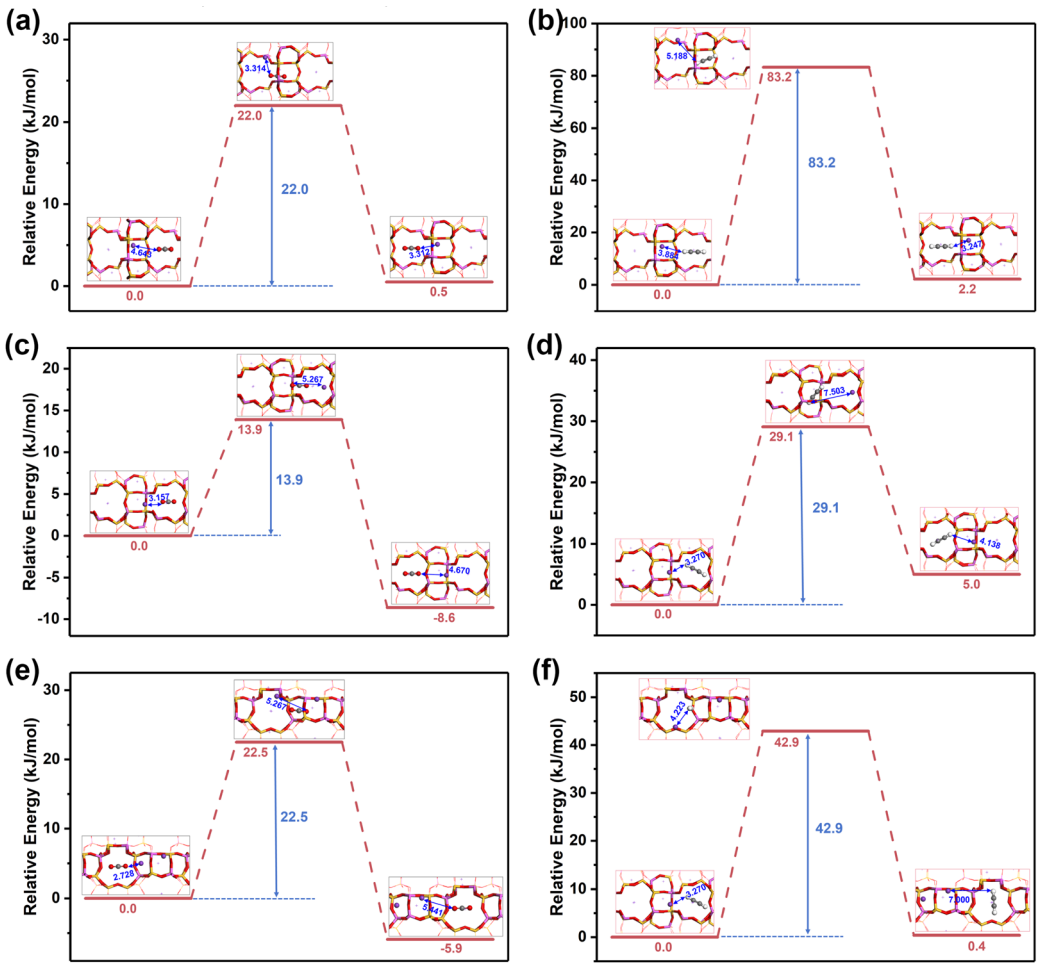


Fig. 5 DFT calculated trapdoor energy barriers for various diffusion pathways. (a and b) Energy barrier diagrams for the diffusion of $CO_2$ (a) and $C_2H_2$ (b) driving the migration of potassium ions (trapdoor effect) *via* pathway I. (c and d) Energy barrier diagrams for the diffusion of $CO_2$ (c) and $C_2H_2$ (d) driving the migration of potassium ions *via* pathway II. (e and f) Energy barrier diagrams for the diffusion of $CO_2$ (e) and $C_2H_2$ (f) driving the migration of potassium ions *via* pathway III. Herein, yellow, pink, red, purple, gray, and white represent silicon, aluminum, oxygen, potassium, carbon, and hydrogen atoms, respectively.

the contracted K-MER-2.0 framework to the expanded framework for $CO_2$ adsorption was only −37.6 kJ $mol^{-1}$, significantly lower than that for $C_2H_2$. These theoretical models were based on a previously reported K-MER structure with a closely matched Si/Al ratio.[17] These computational findings were in good agreement with the experimental observations, demonstrating that K-MER-2.0 undergoes selective framework expansion during $CO_2$ adsorption while maintaining a constricted pore geometry that effectively excludes $C_2H_2$. Notably, the K-MER-2.0 framework remains in an expanded state throughout the $CO_2/C_2H_2$ dynamic breakthrough process due to the presence of $CO_2$. However, $C_2H_2$ remains difficult to adsorb by the swollen K-MER-2.0 framework ($C_2H_2$ dynamic uptake: 5.38 $cm^3$ $g^{-1}$). To further investigate this phenomenon, we conducted additional DFT calculations based on the expanded structural model of the K-MER framework. It is well established that the K-MER structure contains three distinct gas diffusion pathways: (i) from the *d8r* cage to the *pau* cage (denoted Pathway I), (ii) between adjacent ste cages (denoted Pathway II), and (iii) from the ste cage to the *pau* cage (denoted Pathway III) (Fig. S21). All cage-type structures along the diffusion pathways are interconnected through an 8-membered ring (8 MR). Meanwhile, although the K-MER framework remains in an expanded state during $CO_2/C_2H_2$ dynamic breakthrough, the potassium ($K^+$) ions located within the 8 MR continue to play a "trapdoors" role throughout the breakthrough process. As illustrated in Fig. 5a–f and Table S9, the energy barriers for $CO_2$ to displace $K^+$ ions along all three diffusion pathways (Pathway I: 22.0 kJ $mol^{-1}$; Pathway II: 13.9 kJ mol; Pathway III: 22.5 kJ $mol^{-1}$) are significantly lower than those for $C_2H_2$ (Pathway I: 83.2 kJ $mol^{-1}$; Pathway II: 29.1 kJ $mol^{-1}$; Pathway III: 42.9 kJ $mol^{-1}$). These DFT calculations reveal that, even when the K-MER framework is in an expanded state, $C_2H_2$ remains more difficult to adsorb by K-MER compared to $CO_2$, which is consistent with the ultralow $C_2H_2$ uptake (5.38 $cm^3$ $g^{-1}$) and remarkable $CO_2/C_2H_2$ separation factor (12.1) observed in the $CO_2/C_2H_2$ (50/50, v/v, 4 mL $min^{-1}$) breakthrough experiments at 298 K. The cation gating–breathing synergetic mechanism of the material enables preferential accommodation of $CO_2$ molecules while effectively excluding $C_2H_2$, establishing a novel mechanism for gas separation that combines molecular sieving with framework adaptability.

## Conclusions

In summary, we have successfully demonstrated the organic-template-free synthesis of a K-MER-2.0 zeolite that exhibits unprecedented $CO_2/C_2H_2$ reverse separation performance *via* a unique cation-gating and breathing synergistic mechanism. The material exhibits a $CO_2$ adsorption capacity of 70.9 $cm^3$ $g^{-1}$ at 298 K and 101 kPa, along with exceptional separation metrics, including a $CO_2/C_2H_2$ uptake ratio of 13.4 and record-breaking IAST selectivity of 3056. More importantly, the K-MER-2.0 zeolite delivers a high dynamic adsorption capacity of 65.1 $cm^3$ $g^{-1}$ and separation factor of 12.1, which enable single-step $C_2H_2$ production of 1872 mmol $kg^{-1}$ with 99.6% purity, surpassing conventional energy-intensive purification methods. Mechanistic studies reveal $CO_2$-triggered cooperative cation-gated breathing behavior, where selective pore activation occurs exclusively for $CO_2$ adsorption, while also maintaining pore closure against $C_2H_2$ molecules. The excellent selective adsorption capacity could be further extended to other $CO_2$/hydrocarbon systems. The practical viability of the K-MER-2.0 zeolite is further enhanced by efficient adsorption kinetics, exceptional moisture stability, and outstanding regenerability. Critically, the organic-template-free synthesis protocol enables cost-efficient production, positioning K-MER-2.0 as a viable industrial candidate for scalable applications. This work establishes a new paradigm for gas separation through stimulus-responsive pore modulation, simultaneously advancing both industrial gas purification technologies and a fundamental understanding of dynamic molecular sieving with zeolitic materials.

## Author contributions

R. L. and C. L. conceived the research design and drafted the initial manuscript; L. L. and J. H. performed sample characterization; D. M., W. B., and X. Z. carried out theoretical calculations; and X. S. and Z. L. supervised the project and revised the manuscript.

## Conflicts of interest

The authors declare no conflicts of interest.

## Data availability

The data supporting this article have been included as part of the supplementary information (SI). Supplementary Information: experimental details and characterization of the adsorbent. See DOI: **https://doi.org/10.1039/d5sc03281d**.

## Acknowledgements

This work was supported by the National Key Research and Development Program (no. 2023YFB3810700), the National Natural Science Foundation of China (22375070 and 22288101), and the "111 Center" (B17020). We also thank the Shanghai Synchrotron Radiation Facility of BL17UM (**https://cstr.cn/31124.02.SSRF.BL17UM**) for assistance with experimental measurements.

## References

1 Z. Zhang, Z. Deng, H. A. Evans, D. Mullangi, C. Kang, S. B. Peh, Y. Wang, C. M. Brown, J. Wang, P. Canepa, A. K. Cheetham and D. Zhao, Exclusive Recognition of $CO_2$ from Hydrocarbons by Aluminum Formate with Hydrogen-Confined Pore Cavities, *J. Am. Chem. Soc.*, 2023, **145**, 11643–11649.

2 B. Ma, D. Li, Q. Zhu, Y. Li, W. Ueda and Z. Zhang, A Zeolitic Octahedral Metal Oxide with Ultra-Microporosity for Inverse

$CO_2/C_2H_2$ Separation at High Temperature and Humidity, *Angew. Chem., Int. Ed.*, 2022, **61**, e202209121.

3 K. J. Chen, H. S. Scott, D. G. Madden, T. Pham, A. Kumar, A. Bajpai, M. Lusi, K. A. Forrest, B. Space, J. J. Perry and M. J. Zaworotko, Benchmark $C_2H_2/CO_2$ and $CO_2/C_2H_2$ Separation by Two Closely Related Hybrid Ultramicroporous Materials, *Chem*, 2016, **1**, 753–765.

4 S. Liu, X. Han, Y. Chai, G. Wu, W. Li, J. Li, I. Da Silva, P. Manuel, Y. Cheng, L. L. Daemen, A. J. Ramirez-Cuesta, W. Shi, N. Guan, S. Yang and L. Li, Efficient Separation of Acetylene and Carbon Dioxide in a Decorated Zeolite, *Angew. Chem., Int. Ed.*, 2021, **60**, 6526–6532.

5 S. Liu, X. Lian, B. Yue, S. Xu, G. Wu, Y. Chai, Y. Zhang and L. Li, Control of Zeolite Local Polarity toward Efficient Xenon/Krypton Separation, *J. Am. Chem. Soc.*, 2024, **146**, 8335–8342.

6 Y. Zhou, J. Zhang, L. Wang, X. Cui, X. Liu, S. S. Wong, H. An, N. Yan, J. Xie, C. Yu, P. Zhang, Y. Du, S. Xi, L. Zheng, X. Cao, Y. Wu, Y. Wang, C. Wang, H. Wen, L. Chen, H. Xing and J. Wang, Self-Assembled Iron-Containing Mordenite Monolith for Carbon Dioxide Sieving, *Science*, 2021, **373**, 315–320.

7 S. Foorginezhad, F. Weiland, Y. Chen, S. Hussain and X. Ji, Review and Analysis of Porous Adsorbents for Effective $CO_2$ Capture, *Renewable Sustainable Energy Rev.*, 2025, **215**, 115589.

8 S. Q. Yang, R. Krishna, H. Chen, L. Li, L. Zhou, Y. F. An, F. Y. Zhang, Q. Zhang, Y. H. Zhang, W. Li, T. L. Hu and X. H. Bu, Immobilization of the Polar Group into an Ultramicroporous Metal–Organic Framework Enabling Benchmark Inverse Selective $CO_2/C_2H_2$ Separation with Record $C_2H_2$ Production, *J. Am. Chem. Soc.*, 2023, **145**, 13901–13911.

9 O. T. Qazvini, R. Babarao and S. G. Telfer, Selective Capture of Carbon Dioxide from Hydrocarbons Using a Metal–Organic Framework, *Nat. Commun.*, 2021, **12**, 197.

10 Y. Gu, J. Zheng, K. Otake, M. Shivanna, S. Sakaki, H. Yoshino, M. Ohba, S. Kawaguchi, Y. Wang, F. Li and S. Kitagawa, Host–Guest Interaction Modulation in Porous Coordination Polymers for Inverse Selective $CO_2/C_2H_2$ Separation, *Angew. Chem., Int. Ed.*, 2021, **60**, 11688–11694.

11 L. Cai, Z. Yao, S. Lin, M. Wang and G. Guo, Photoinduced Electron-Transfer (PIET) Strategy for Selective Adsorption of $CO_2$ over $C_2H_2$ in a MOF, *Angew. Chem., Int. Ed.*, 2021, **60**, 18223–18230.

12 X. Han and S. Yang, Molecular Mechanisms behind Acetylene Adsorption and Selectivity in Functional Porous Materials, *Angew. Chem., Int. Ed.*, 2023, **62**, e202218274.

13 J. Jia, N. Yan, X. Lian, S. Liu, B. Yue, Y. Chai, G. Wu, J. Xu and L. Li, Molecular Trapdoor in HEU Zeolite Enables Inverse $CO_2$-$C_2H_2$ Separation, *Angew. Chem., Int. Ed.*, 2025, **64**, e202419091.

14 G. Deng, K. Cheng, B. Meng, X. Shi, X. Liu, Y. Zhou and J. Wang, Regulating the Si/Al Ratio of GIS Zeolite with Bulky Primary Particles for Selective $CO_2$ Capture from Hydrocarbons, *Sep. Purif. Technol.*, 2024, **340**, 126764.

15 X. Zhang, Y. Wang, L. Yang, X. Lu, X. Suo, X. Cui and H. Xing, Efficient Kinetic Separation of Carbon Dioxide from Acetylene Using Mordenites Featuring Modified 1D Channels with Excellent Selectivity and Diffusion, *Adv. Mater.*, 2025, **37**, 2501870.

16 V. M. Georgieva, E. L. Bruce, M. C. Verbraeken, A. R. Scott, W. J. Casteel, S. Brandani and P. A. Wright, Triggered Gate Opening and Breathing Effects during Selective $CO_2$ Adsorption by Merlinoite Zeolite, *J. Am. Chem. Soc.*, 2019, **141**, 12744–12759.

17 H. J. Choi, D. Jo, J. G. Min and S. B. Hong, The Origin of Selective Adsorption of $CO_2$ on Merlinoite Zeolites, *Angew. Chem., Int. Ed.*, 2021, **60**, 4307–4314.

18 E. L. Bruce, V. M. Georgieva, M. C. Verbraeken, C. A. Murray, M.-F. Hsieh, W. J. Casteel, A. Turrina, S. Brandani and P. A. Wright, Structural Chemistry, Flexibility, and $CO_2$ Adsorption Performance of Alkali Metal Forms of Merlinoite with a Framework Si/Al Ratio of 4.2, *J. Phys. Chem. C*, 2021, **125**, 27403–27419.

19 H. Lee, D. Xie, S. I. Zones and A. Katz, $CO_2$ Desorbs Water from K-MER Zeolite under Equilibrium Control, *J. Am. Chem. Soc.*, 2024, **146**, 68–72.

20 MER: XPD Pattern, **https://europe.iza-structure.org/IZA-SC/pow_pat.php?ID=178**, accessed April 21, 2025.

21 B. M. Skofteland, O. H. Ellestad and K. P. Lillerud, Potassium Merlinoite: Crystallization, Structural and Thermal Properties, *Microporous Mesoporous Mater.*, 2001, **43**, 61–71.

22 X. Tang, M. Wei, X. Bai, J. Li and J. Yang, Precise Pore Size Modulation of K-MER Zeolites for $N_2$ Trapping, *Sep. Purif. Technol.*, 2024, **339**, 126601.

23 D. Fu and M. E. Davis, Carbon Dioxide Capture with Zeotype Materials, *Chem. Soc. Rev.*, 2022, **51**, 9340–9370.

24 F. Akhtar, Q. Liu, N. Hedin and L. Bergström, Strong and Binder Free Structured Zeolite Sorbents with Very High $CO_2$-over-$N_2$ Selectivities and High Capacities to Adsorb $CO_2$ Rapidly, *Energy Environ. Sci.*, 2012, **5**, 7664.

25 H. J. Choi, E. L. Bruce, K. S. Kencana, J. Hong, P. A. Wright and S. B. Hong, Highly Cooperative $CO_2$ Adsorption via a Cation Crowding Mechanism on a Cesium-Exchanged Phillipsite Zeolite, *Angew. Chem., Int. Ed.*, 2023, **62**, e202305816.

26 S. Geng, H. Xu, C. Cao, T. Pham, B. Zhao and Z. Zhang, Bioinspired Design of a Giant $[Mn_{86}]$ Nanocage-Based Metal–Organic Framework with Specific $CO_2$ Binding Pockets for Highly Selective $CO_2$ Separation, *Angew. Chem., Int. Ed.*, 2023, **62**, e202305390.

27 L. Li, J. Wang, Z. Zhang, Q. Yang, Y. Yang, B. Su, Z. Bao and Q. Ren, Inverse Adsorption Separation of $CO_2/C_2H_2$ Mixture in Cyclodextrin-Based Metal–Organic Frameworks, *ACS Appl. Mater. Interfaces*, 2019, **11**, 2543–2550.

28 S.-M. Wang, M. Shivanna, S. T. Zheng, T. Pham, K. A. Forrest, Q. Y. Yang, Q. Guan, B. Space, S. Kitagawa and M. J. Zaworotko, Ethane/Ethylene Separations in Flexible Diamondoid Coordination Networks via an Ethane-Induced Gate-Opening Mechanism, *J. Am. Chem. Soc.*, 2024, **146**, 4153–4161.

29 Y. Chai, X. Han, W. Li, S. Liu, S. Yao, C. Wang, W. Shi, I. da-Silva, P. Manuel, Y. Cheng, L. D. Daemen, A. J. Ramirez-Cuesta, C. C. Tang, L. Jiang, S. Yang, N. Guan and L. Li, Control of Zeolite Pore Interior for Chemoselective Alkyne/Olefin Separations, *Science*, 2020, **368**, 1002–1006.

30 Z. Zhang, S. B. Peh, R. Krishna, C. Kang, K. Chai, Y. Wang, D. Shi and D. Zhao, Optimal Pore Chemistry in an Ultramicroporous Metal–Organic Framework for Benchmark Inverse $CO_2/C_2H_2$ Separation, *Angew. Chem., Int. Ed.*, 2021, **60**, 17198–17204.

31 C. He, P. Zhang, Y. Wang, Y. Zhang, T. Hu, L. Li and J. Li, Thermodynamic and Kinetic Synergetic Separation of $CO_2$/$C_2H_2$ in an Ultramicroporous Metal–Organic Framework, *Sep. Purif. Technol.*, 2023, **304**, 122318.

32 Q. Liu, S. G. Cho, J. Hilliard, T. Wang, S. Chien, L. Lin, A. C. Co and C. R. Wade, Inverse $CO_2/C_2H_2$ Separation with MFU-4 and Selectivity Reversal via Postsynthetic Ligand Exchange, *Angew. Chem., Int. Ed.*, 2023, **62**, e202218854.

33 Y. Xie, H. Cui, H. Wu, R. Lin, W. Zhou and B. Chen, Electrostatically Driven Selective Adsorption of Carbon Dioxide over Acetylene in an Ultramicroporous Material, *Angew. Chem., Int. Ed.*, 2021, **60**, 9604–9609.

34 H. June Choi, D. Jo and S. Bong Hong, Effect of Framework Si/Al Ratio on the Adsorption Mechanism of $CO_2$ on Small-Pore Zeolites: II. Merlinoite, *Chem. Eng. J.*, 2022, **446**, 137100.

35 V. M. Georgieva, E. L. Bruce, R. G. Chitac, M. M. Lozinska, A. M. Hall, C. A. Murray, R. I. Smith, A. Turrina and P. A. Wright, Cation Control of Cooperative $CO_2$ Adsorption in Li-Containing Mixed Cation Forms of the Flexible Zeolite Merlinoite, *Chem. Mater.*, 2021, **33**, 1157–1173.

36 D. Yang, H. V. Doan, U. O'Hara, D. Reed, J. Hungerford, J. C. Eloi, N. E. Pridmore, P. F. Henry, S. Rochat, M. Tian and V. P. Ting, Impact of Cations and Framework on Trapdoor Behavior: A Study of Dynamic and In Situ Gas Analysis, *Langmuir*, 2024, **40**, 12394–12406.